Research Square

Preprints are preliminary reports that have not undergone peer review.
They should not be considered conclusive, used to inform clinical practice,
or referenced by the media as validated information.

Climate Warming Accelerates Hydrological Reversals Across Europe

Ray Kettaren

kettaren@fzp.czu.cz

Czech University of Life Sciences Prague https://orcid.org/0009-0000-2338-3209

Rohini Kumar

Helmholtz Centre for Environmental Research - UFZ https://orcid.org/0000-0002-4396-2037

Devvrat Yadav

Czech University of Life Sciences https://orcid.org/0009-0002-1171-7261

Miroslav Trnka

Global Change Research Institute CAS

Martin Hanel

Czech University of Life Sciences Prague https://orcid.org/0000-0001-8317-6711

Amir AghaKouchak

University of California, Irvine https://orcid.org/0000-0003-4689-8357

Oldrich Rakovec

Faculty of Environmental Sciences, Czech University of Life Sciences Prague https://orcid.org/0000-0003-2451-3305

Article

Keywords:

Posted Date: June 22nd, 2026

DOI: https://doi.org/10.21203/rs.3.rs-9924236/v1

License: This work is licensed under a Creative Commons Attribution 4.0 International License.
Read Full License

Additional Declarations: There is **NO** Competing Interest.

Climate Warming Accelerates Hydrological Reversals Across Europe

Ray Kettaren[1,*], Rohini Kumar[2,*], Devvrat Yadav[1], Miroslav Trnka[3,4], Martin Hanel[1,5], Amir AghaKouchak[6,7,8], and Oldrich Rakovec[1,*]

[1]Faculty of Environmental Sciences, Czech University of Life Sciences Prague, Praha-Suchdol, Czech Republic

[2]UFZ-Helmholtz Centre for Environmental Research, Leipzig, Germany

[3]Department of Agrosystems and Bioclimatology, Mendel University in Brno, Brno, 63132, Czech Republic

[4]Global Change Research Institute of the Czech Academy of Sciences, Brno, 60300, Czech Republic

[5]T.G. Masaryk Water Research Institute, Podbabska 30, Praha 6, 16000, Czech Republic

[6]Department of Civil and Environmental Engineering, University of California, Irvine, CA, USA

[7]Department of Earth System Science, University of California, Irvine, CA, USA

[8]United Nations University Institute for Water, Environment and Health (UNU-INWEH), Richmond Hill, Ontario, Canada

[*]Corresponding Authors: kettaren@fzp.czu.cz, rohini.kumar@ufz.de, rakovec@fzp.czu.cz

Abstract

Low and high river flows are among the most critical challenges in water resource management, with substantial societal, economic, and environmental impacts. Yet, the interconnections between these two opposing low- and high-flow episodes are rarely examined simultaneously, limiting understanding of how their contrasting responses to warming may compound challenges for adaptation planning. Hydrological simulations driven by bias-corrected climate projections show intensifying low-flow episodes and weakening high-flow episodes across Europe, generating opposing responses over nearly half of the continent as warming increases. Transition times from high- to low-flow episodes shorten by more than a third (from 7.6 to 4.8 months) at 3°C warming, whereas transitions from low- to high-flow episodes lengthen only marginally (6.0 to 6.6 months), revealing an asymmetric response where low-flow conditions arrive faster yet persist longer. This progressively shrinking recovery window challenges drought preparedness, ecosystem recovery, and water allocation strategies in a warming climate.

Climate warming is reshaping river-flow regimes by altering not only the frequency and magnitude of hydrological events, but also the temporal sequencing

of contrasting flow conditions[1]. Human-induced climate change has intensified components of the global water cycle and amplified both wet and dry anomalies across many regions, although evidence for a globally uniform intensification of the hydrological cycle remains mixed[2–4]. At the continental scale, these changes often emerge as divergent streamflow responses, with low-flow conditions intensifying in drying regions and high-flow becoming more frequent or severe in wetter regions[4–7]. Both types of streamflow conditions impose substantial societal and ecological costs, affecting hydropower generation, navigation, irrigation, water supply, infrastructure safety, and riverine ecosystems[8–13]. Yet most assessments continue to examine low- and high-flow conditions separately, leaving their interconnected responses to climate warming largely unexplored. Treating low- and high-flow conditions separately obscures how they co-evolve under warming and whether the interval available for hydrological, ecological, and infrastructural recovery changes between opposing conditions[9,14–16].

Europe provides a critical test case for examining streamflow anomalies because its hydrological regimes exhibit strong regional contrasts under climate variability and change[3]. Observed discharge records show a marked north-south asymmetry, with increasing flood occurrence or severity in parts of northern and northwestern Europe, and intensifying low-flow conditions and drought stress across

southern Europe and the Mediterranean, where declining precipitation and increasing evaporative demand reinforce drying[9,16–19]. Climate projections suggest that spatial divergence will become more pronounced under further warming, with increasing drought stress across the Mediterranean and parts of Central Europe, alongside more frequent or severe high-flow conditions in Northern Europe and parts of western Europe[9,16,20,21]. These contrasting responses reflect a broader European hydroclimatic gradient, with drying tendencies in the Mediterranean and wetting tendencies in Northern Europe. Central Europe forms a transitional region where competing changes in precipitation, evaporative demand, and seasonality can produce spatially heterogeneous streamflow responses[22]. These trajectories indicate that warming reshapes European streamflow episodes unevenly, producing regionally distinct responses that intensify with increasing warming. Strong regional contrasts in European hydrology make the continent an ideal place to test whether warming reshapes not only the locations of low- and high-flow episodes, but also the speed at which river systems shift between them.

Despite substantial progress in characterizing individual streamflow episodes, the timing between opposing low- and high-flow conditions remains insufficiently quantified. Previous studies have shown that drought conditions can influence the timing and severity of subsequent flood events[23], and that rapid dry-to-wet tran-

sitions, often referred to as hydroclimatic whiplash, may intensify under climate warming[24,25]. However, consecutive drought-to-flood transitions remain inconsistently defined, and their timing, occurrence, and spatio-temporal variability are still insufficiently understood[1,26]. Although low-flow and high-flow episodes are not equivalent to droughts and floods, they provide a standardized hydrological basis for assessing shifts between anomalously low and high river-flow conditions. Here, we use the term hydrological reversal to describe the transition between consecutive low- and high-flow episodes, and vice versa. The time interval separating such opposing episodes is critical because it determines whether river systems retain sufficient capacity to recover, replenish water storage, sustain ecological functioning, and maintain infrastructure resilience before the next contrasting episode occurs[15,27].

Here, we assess how progressive climate warming alters low-flow and high-flow episodes and the transition times between them across Europe. We use the mesoscale Hydrological Model (mHM)[28,29], driven by E-OBS-adjusted ISIMIP3b climate forcing[30–32] (see Methods). We quantify changes in the frequency, duration, magnitude, and transition times of low- and high-flow episodes at 1.5°C, 2°C, and 3°C of global warming across Europe and three climatologically distinct regions: Northern Europe (NEU), Central Europe (CEU), and the Mediterranean

(MED)[33]. Low- and high-flow episodes are identified from monthly Standardized Runoff Index-derived non-exceedance probabilities, using thresholds below the 20th and above the 80th percentile of the reference distribution[34,35]. This framework tests whether warming reshapes streamflow regimes not only by altering episode characteristics, but also by changing the interval between opposing hydrological conditions. Furthermore, signal-to-noise ratios are used to quantify the robustness of projected changes across the model ensemble (see Methods).

Results

Divergent responses of streamflow episodes to warming

Characteristics of low- and high-flow episodes (Fig. 1) across Europe highlight contrasting responses to varying levels of climate warming. At the continental scale, high-flow episodes become less frequent under higher warming levels, with median frequency declining by 17% at 3°C relative to the historical reference period (1980–2010), alongside a 14% decrease in cumulative magnitude, while duration increases slightly by ≈3% (Fig. 1a). The combination of fewer high-flow episodes with lower cumulative magnitude that persist for marginally longer suggests a systematic attenuation of sustained high-flow conditions. High-flow fre-

quency and cumulative magnitude decline progressively as warming intensifies: at 1.5°C, all three characteristics show negligible change, but by 3°C, both magnitude and frequency shift clearly toward negative values. This is consistent with observed reductions in European high-flow episodes driven by shifting precipitation seasonality and diminishing snowmelt contributions that redistribute runoff away from peak flow conditions[7,36,37]. Regionally, attenuation is most pronounced in the Mediterranean (MED) region, where high-flow magnitude and frequency decline by more than 50% at the highest warming level (Supplementary Fig. 1a). Northern Europe (NEU) shows the opposite response, with increases in high-flow magnitude, frequency, and duration under warming. In NEU, more frequent high-flow episodes are likely associated with increasing winter precipitation and a shift from snowmelt-driven to rainfall-dominated high-flow regimes in northern catchments[16,17]. CEU occupies a transitional position in which the high-flow signal remains ambiguous, reflecting the competing influences of increasing precipitation intensity and rising evapotranspiration, which partially offset each other[38]. Additionally, absolute values of these characteristics at each warming level are shown in Supplementary Fig. 2; relative changes are presented here to emphasize proportional shifts across warming levels.

Low-flow episodes (Fig. 1b), by contrast, intensify systematically across all

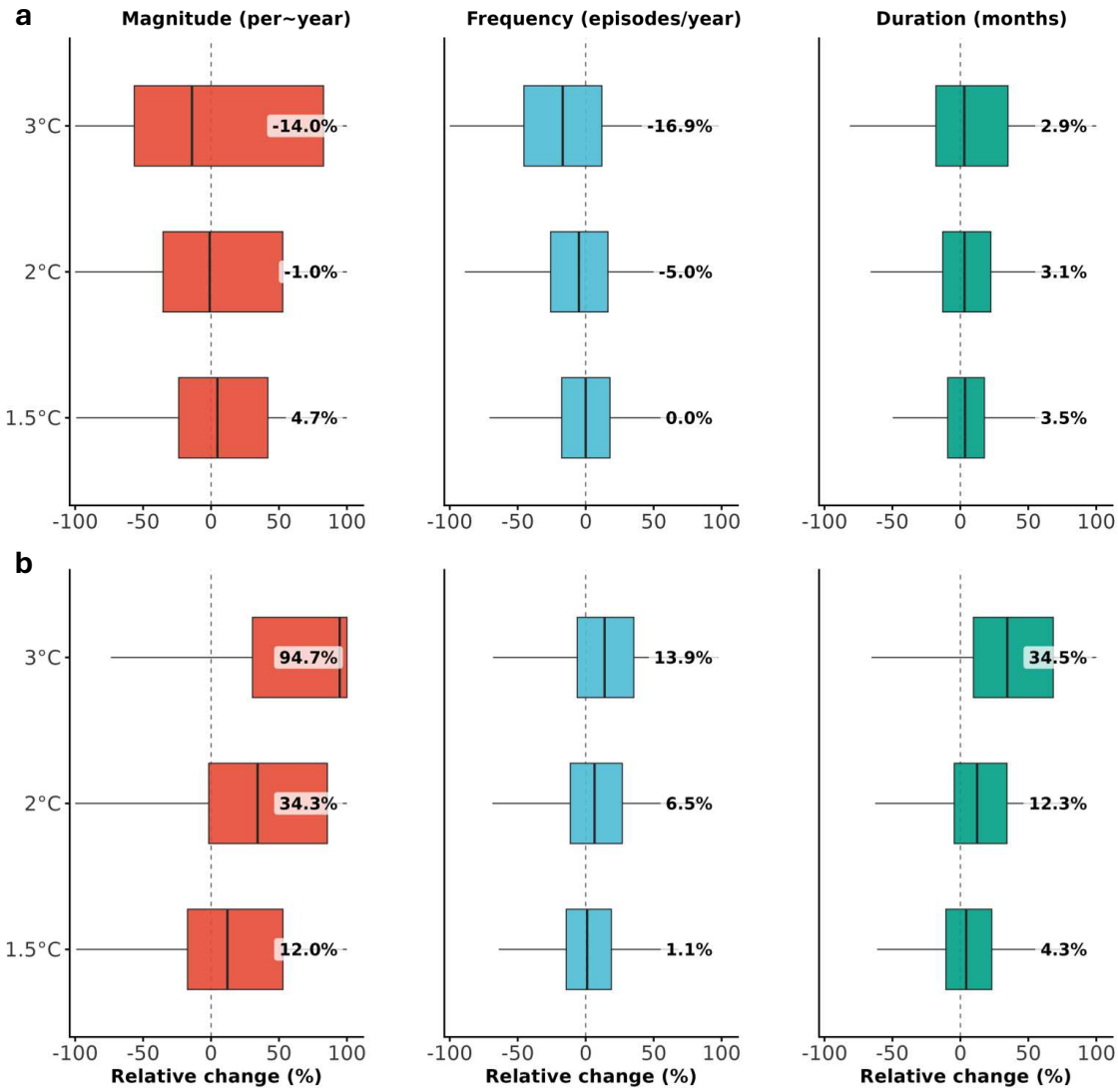


Fig. 1 | **Divergent responses of high- and low-flow episodes to progressive warming across Europe.** Relative changes in magnitude (annual cumulative percentile deficit or surplus), frequency (episodes/year), and duration (months) for high-flow (**a**, top) and low-flow (**b**, bottom) episodes at 1.5°C, 2°C, and 3°C warming relative to the historical reference period (1980–2010). Bars show interquartile range across European pixels; vertical lines indicate median values. Percentage labels denote median relative change.

three characteristics with warming. Median magnitude increases by 12% at 1.5°C and by 95% at 3°C, indicating a strong intensification of low-flow deficit magnitude under progressive warming[9,39]. Frequency and duration increase consistently, with projected rises of 13.9% and 34.5%, respectively, at 3°C. The increase in magnitude becomes stronger at higher warming levels: the increment between 2°C and 3°C (+60%) far exceeds that between 1.5°C and 2°C (+22%), indicating that drying intensification accelerates disproportionately beyond 2°C. This accelerating response is consistent with the finding that at higher warming levels, atmospheric evaporative demand rises faster than precipitation, particularly during summer when the imbalance between supply and demand is largest[18,38,40]. In contrast to the continental-scale attenuation of sustained high-flow episodes, low-flow characteristics intensify systematically, reflecting more frequent, prolonged, and severe streamflow deficits. The intensification is strongest in MED (Supplementary Fig. 1b), where cumulative magnitude exceeds +180% at 3°C, while changes in NEU remain close to zero, consistent with increasing precipitation sustaining streamflow in northern catchments[3]. These contrasting regional responses align with the well-documented north–south hydroclimatic divergence across Europe[3,9,16,41].

In addition, the annual cycle reveals how low-flow and high-flow episodes

diverge seasonally under warming (Supplementary Fig. 3). During the historical period, ≈20% of the European area experiences low- or high-flow conditions in any given month, with little seasonal variation. This reflects the construction of the percentile-based runoff index, in which month-specific Gamma distributions fitted over the 1960–2024 reference period define the climatological 20th- and 80th-percentile thresholds independently for each calendar month and grid cell. A pronounced divergence emerges at 3°C: ≈47% of the continent falls below the low-flow threshold during July and August, while high-flow area fractions decline to about 10% in those months but increase to 30% during winter. Seasonal redistribution is consistent with enhanced evaporative demand and the declining role of snowmelt in sustaining summer high-flow conditions under warming[17]. These results highlight the intensification of low-flow conditions, which is concentrated during the warm season when evaporative demand is highest[40]. Moreover, these conditions should be viewed from a large-scale perspective, as the analysis aggregates results across Europe, potentially masking local-scale differences in drying and wetting patterns.

The disparity between low-flow and high-flow responses also reflects strong spatial heterogeneity. The interquartile ranges of projected high-flow (Fig. 1a) changes remain broad across all warming levels, with boxes spanning both pos-

itive and negative values for magnitude and frequency even at 3°C, showing the influences of precipitation, evapotranspiration, and snowmelt dynamics across Europe's diverse hydroclimatic regions[42,43]. Low-flow changes shift more consistently toward positive values by 3°C, reflecting the broad expansion of low-flow intensification across southern and central Europe. Model-based robustness is assessed separately using signal-to-noise ratios (Supplementary Fig. 4). It should be noted that our analysis characterizes moderate flow anomalies defined by the 20th and 80th percentiles of the reference distribution. Although the balance between low- and high-flow responses may differ for rarer extremes, the overall patterns remain consistent when stricter percentile thresholds are applied using the 10th percentile for low-flow and the 90th percentile for high-flow (Supplementary Fig. 5).

Low- and high-flow frequency changes across Europe

Consistent with observed large-scale changes in river flow[3], projected frequency changes reveal pronounced regional differences in the responses of low- and high-flow episodes to warming (Fig. 2). Low-flow frequency increases are concentrated in the Mediterranean basin, the Iberian Peninsula, southern France, Italy, and the Balkans, where projected changes exceed 50% by 3°C, with poten-

tial consequences for basin-scale water supply, ecosystems, and drought management. High-flow frequency shows an opposing spatial pattern, with increases in NEU and pronounced decreases across MED, broadly consistent with multi-model projections of European high-flow conditions and flood-related changes under warming[16]. These changes reflect the established north–south hydroclimatic gradient, with Central Europe positioned between a wetter Scandinavia and a drier Mediterranean, where model projections remain especially uncertain[41,44–46].

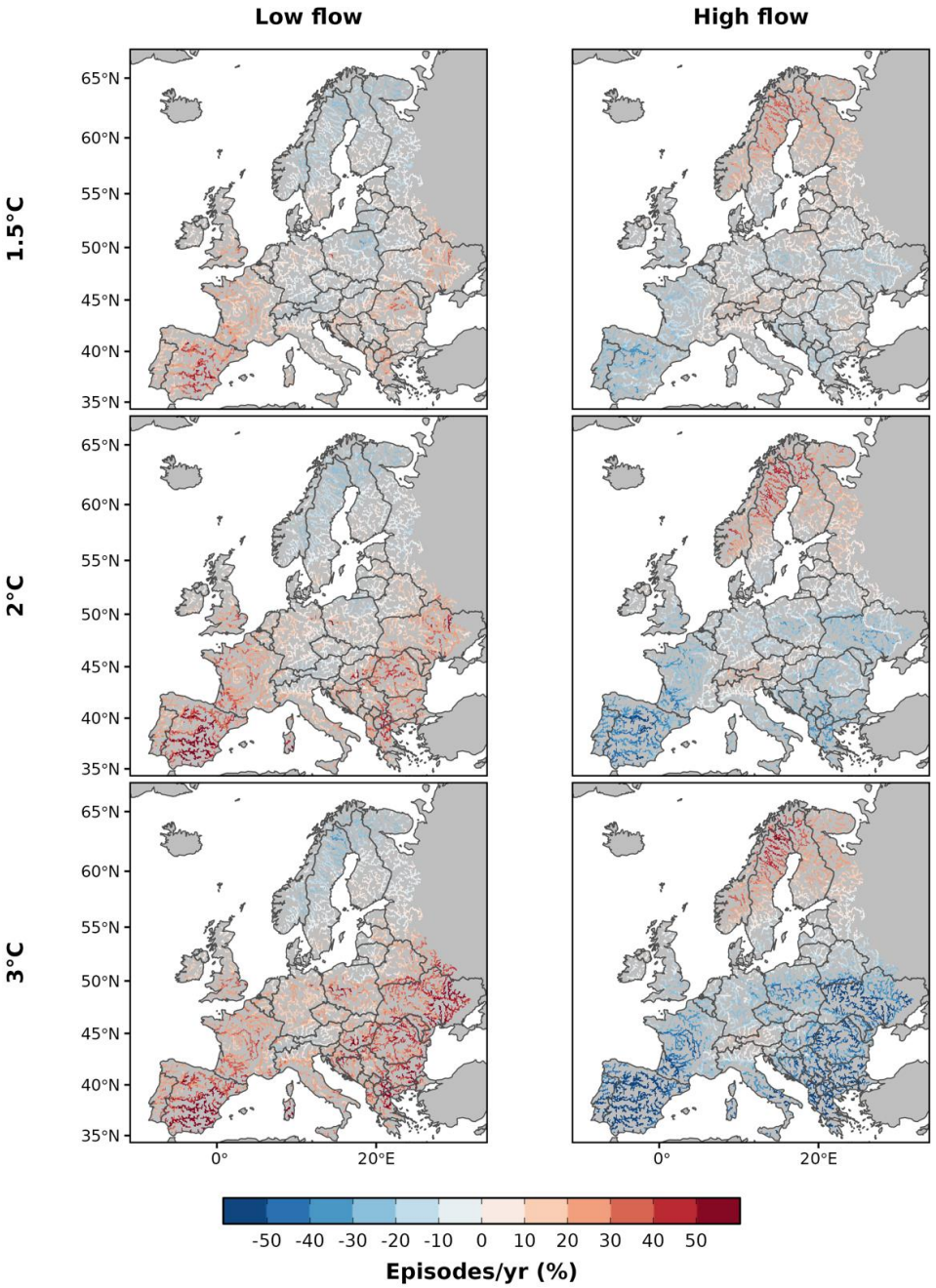


Fig. 2 | Spatial relative changes in low- and high-flow frequency under climate warming. Relative changes in frequency for low-flow (left column) and high-flow (right column) episodes. Blue shading indicates declining frequency; red indicates increasing frequency.

193 At 1.5°C, projected frequency changes remain weak across much of Eu-
194 rope, but by 2°C and particularly 3°C, high-flow decreases become widespread
195 across southern and central Europe, while localized increases appear in Scandi-
196 navia, likely linked to intensifying winter precipitation and the shift from snowmelt-
197 dominated to rainfall-dominated high-flow regimes[17]. CEU occupies a transitional
198 position in which competing hydroclimatic drivers suppress the emergence of a
199 clear directional signal. Spatial significance testing shows that robust frequency
200 changes expand with warming (Supplementary Fig. 6). At 3°C, low-flow increases
201 become significant across much of southern Europe and parts of Central Europe,
202 while high-flow changes show significant decreases across southern and central
203 Europe and increases in Scandinavia.

204 More frequent low-flow conditions likely arise from declining summer precip-
205 itation and increasing evaporative demand in southern Europe, reinforcing recur-
206 rent drought conditions[18,20,47]. In NEU, low-flow frequency generally decreases,
207 with the strongest signal at the highest warming level, in line with projected in-
208 creases in annual precipitation that help sustain discharge[3]. CEU shows mixed
209 signals of both increases and decreases, confirming its role as a transitional zone
210 where the combined effects of increased winter and spring precipitation and rising
211 summer evapotranspiration partially offset each other[38]. This regional ambiguity is

also consistent with the strong interannual variability of Central European summer rainfall, including recently identified links to remote oceanic forcing via the Pacific Meridional Mode[48]. The spatial pattern shifts from weak and fragmented signals at 1.5°C warming to a pronounced north–south dipole at 3°C warming. This suggests that limiting warming to 1.5°C could reduce the spatial extent of increased low-flow frequency.

Moreover, spatial patterns of magnitude and duration changes (Supplementary Fig. 7) are broadly consistent with frequency results. Low-flow magnitude intensifies across southern and central Europe, while high-flow magnitude declines in the same regions but increases in NEU. Regarding duration changes, low-flow conditions persist longer (green shaded) in CEU and MED, whereas they become shorter in NEU (orange shaded). Consistently, high-flow conditions last longer in NEU and become shorter in MED, with CEU showing only marginal increases in duration. Shifts in magnitude and duration are central to water management, providing key information for climate adaptation strategies and for assessing flood and drought risks across both high- and low-flow regimes.

Opposing change directions of low- and high-flow across Europe

To assess the co-occurrence of divergent frequency changes in low-flow and high-flow conditions, each grid cell was categorized based on the direction of statistically significant change in both episodes (H+/H$-$ for high-flow increase/decrease and L+/L$-$ for low-flow increase/decrease; see Methods). Fig. 3 shows the spatial distribution and areal extent of combined low- and high-flow frequency changes at 3°C, where the signal is strongest. The dominant category is L$+$, H$-$, covering 46% of European river grid cells. In these regions, low-flow frequency increases while high-flow frequency decreases, with the pattern spanning the Iberian Peninsula, southern France, Italy, and large parts of eastern Europe. The opposite category, L$-$, H$+$, covers 11.7% of river grid cells and is mainly concentrated in NEU and the Baltic region, indicating increasing high-flow frequency alongside decreasing low-flow frequency. The two same-direction categories (L$+$, H$+$ and L$-$, H$-$) are absent under this category, suggesting that robust low- and high-flow frequency changes rarely occur in the same direction. The remaining 42% of river grid cells are not jointly significant for both episode types and are concentrated mainly across Central Europe, which acts as a transitional zone. This absence of a jointly significant signal should not be interpreted as stability, but rather as reflecting uncertainty in how competing hydroclimatic drivers balance under future warming.

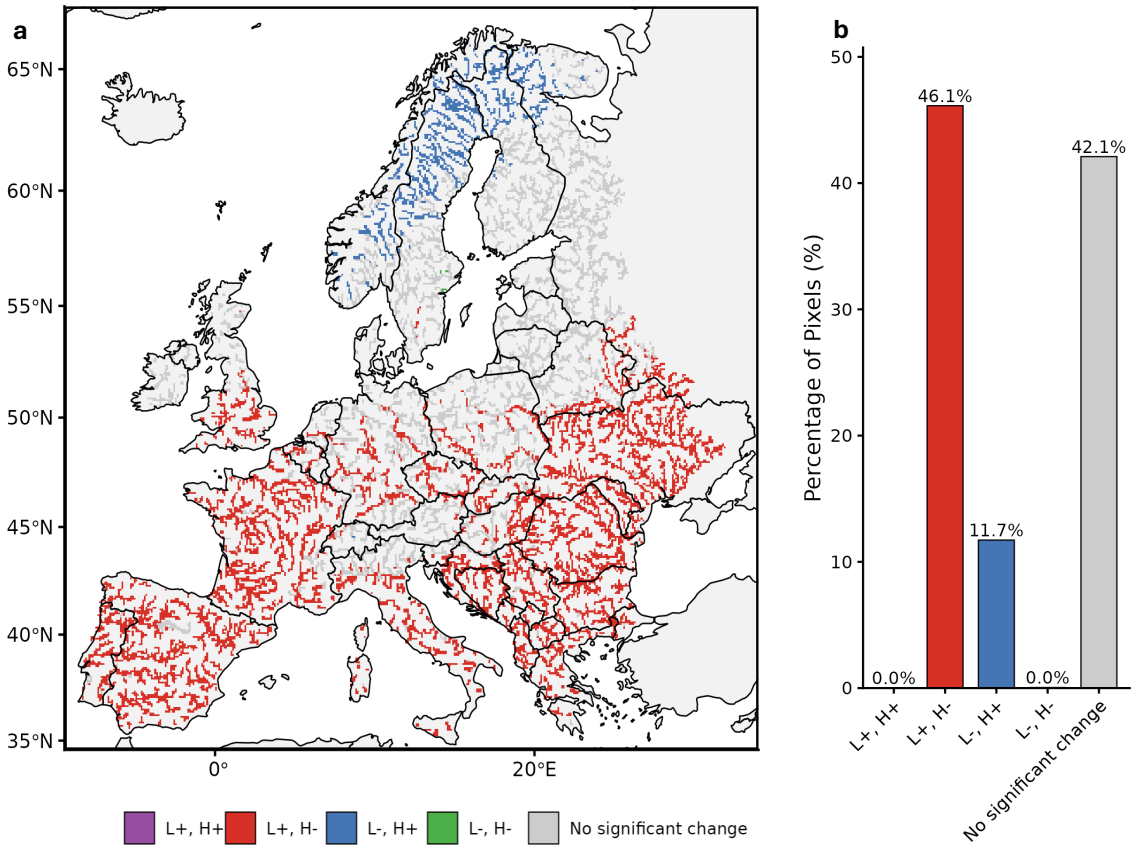


Fig. 3 | Change-direction categories for low- and high-flow conditions at 3°C warming. Spatial distribution (**a**) and areal percentages (**b**) of river grid cells exhibiting significant changes ($p < 0.05$, Wilcoxon signed-rank test) in low- (L) and high-flow (H) condition frequency at 3°C warming relative to reference baseline (1980–2010). River grid cells are grouped into five categories: L+, H+ (both increasing), L+, H− (low-flow increasing, high-flow decreasing), L−, H+ (low-flow decreasing, high-flow increasing), L−, H− (both decreasing), and no jointly significant change. A river grid cell is grouped as having significant change only when both low- and high-flow changes are individually significant at $p < 0.05$.

The dominance of the L+, H− category across large parts of CEU and MED is consistent with the combined effects of declining warm-season precipitation[3],

rising atmospheric evaporative demand[18], increasing snow drought[37], and diminishing snowmelt contributions[17] under warming. In these regions, reduced summer precipitation and intensified evapotranspiration jointly promote more frequent below-threshold streamflow conditions[40,49,50], while declining snow accumulation and earlier melt timing redistribute streamflow away from the seasonal peak-flow period, reducing high-flow occurrence[38]. In large parts of NEU, where the L$-$, H$+$ class prevails, increasing annual precipitation partly offsets evapotranspiration losses, supporting fewer low-flow episodes while increasing rainfall-driven high-flow episodes as snowmelt-dominated regimes shift toward more pluvial regimes[3,7,17]. The opposing responses of low-flow and high-flow episodes therefore reflect shared hydroclimatic drivers (e.g., precipitation, evapotranspiration, and snowmelt) that favour more frequent low-flow conditions and fewer sustained high-flow episodes in southern Europe, with the opposite tendency in the north. This classification relies solely on frequency changes; alternative metrics, such as magnitude or duration, may reveal different spatial patterns where episode characteristics evolve in different directions.

Asymmetric shifts in transition times between streamflow episodes

We define transition time as the median number of months between the end

of one episode type and the onset of the opposite condition, calculated separately for low→high and high→low transitions (see Methods and Fig. 4a,b). At the continental scale, the two transition directions respond asymmetrically to continuous warming. The low→high transition time increases modestly from 6.0 months in the historical period to 6.6 months at 3°C, while the high→low transition time decreases sharply from 7.6 to 4.8 months over the same warming range (Fig. 4a). Thus, warming slightly lengthens the interval before high-flow conditions return after low-flow episodes, but strongly shortens the interval before low-flow conditions return after a high-flow episode. The transition-class distributions further highlight this asymmetry (Fig. 4b). High→low transitions shift toward more abrupt timing, with the abrupt class accounting for approximately 60% of European river grid cells at 3°C. In contrast, low→high transitions show increases in both abrupt and gradual classes, consistent with a weaker and more heterogeneous change in transition timing.

The compression of high→low transition time represents the most pronounced temporal change identified in this study. The reduction from 7.6 months under historical conditions to 4.8 months at 3°C corresponds to a ≈37% shortening of the interval between a high-flow condition and the next low-flow condition. This means that, at the highest warming level, low-flow conditions emerge nearly three

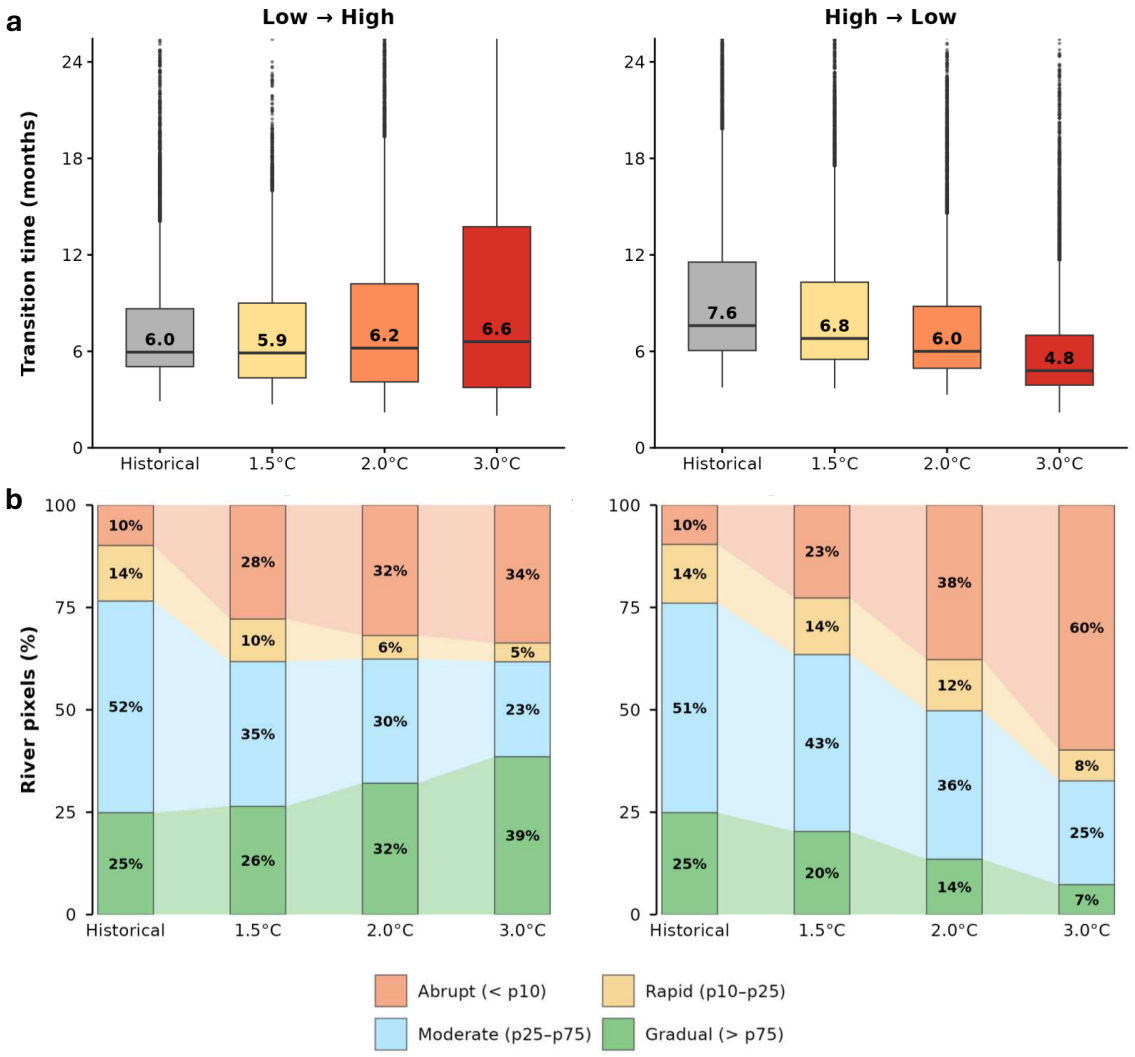


Fig. 4 | Transition times between opposing streamflow episodes under progressive warming. Median transition times across river grid cells (**a**) and transition-class distributions (**b**), based on transition-time percentiles derived from the 1980–2010 reference period. The left column represents low→high transitions and the right column high→low transitions. Transitions are classified as Abrupt ($<$ p10), Rapid (p10–p25), Moderate (p25–p75), and Gradual ($>$ p75). In panel (**b**), percentages denote river grid cells coverage, while flow widths indicate redistribution among transition categories.

months sooner after high-flow episodes than under historical conditions. The compression is progressive: transition time decreases by 0.8 months between the historical period and 1.5°C, by a further 0.8 months between 1.5°C and 2°C, and by a further 1.2 months between 2°C and 3°C, indicating that the contraction strengthens at higher warming levels. Physically, this shortening may be associated with increased atmospheric evaporative demand under warming, which can accelerate streamflow depletion during normal-flow conditions following a high-flow episode[51]. However, precipitation timing and snow storage changes may also influence this transition, suggesting that evaporative demand alone may not fully explain the local water balance response. In practical terms, the results suggest a reduced interval following high-flow episodes during which reservoir storage, soil moisture, and groundwater may be replenished before low-flow conditions recur. This may affect water supply planning, agriculture, and reservoir operations[8].

The spatial distributions of transition times (Supplementary Fig. 8) reveal substantial regional variation beneath the continental medians. For the high$\rightarrow$low direction (bottom row), the shortest transition times (below 6 months) are concentrated across southern and central Europe, with values dropping below 3 months in parts of the Mediterranean and the Balkans by 3°C. These areas largely overlap with regions categorized under the L$+$, H$-$ change direction (Fig. 3), implying spa-

tial coherence between where low-flow conditions intensify and where they return faster after high-flow conditions.

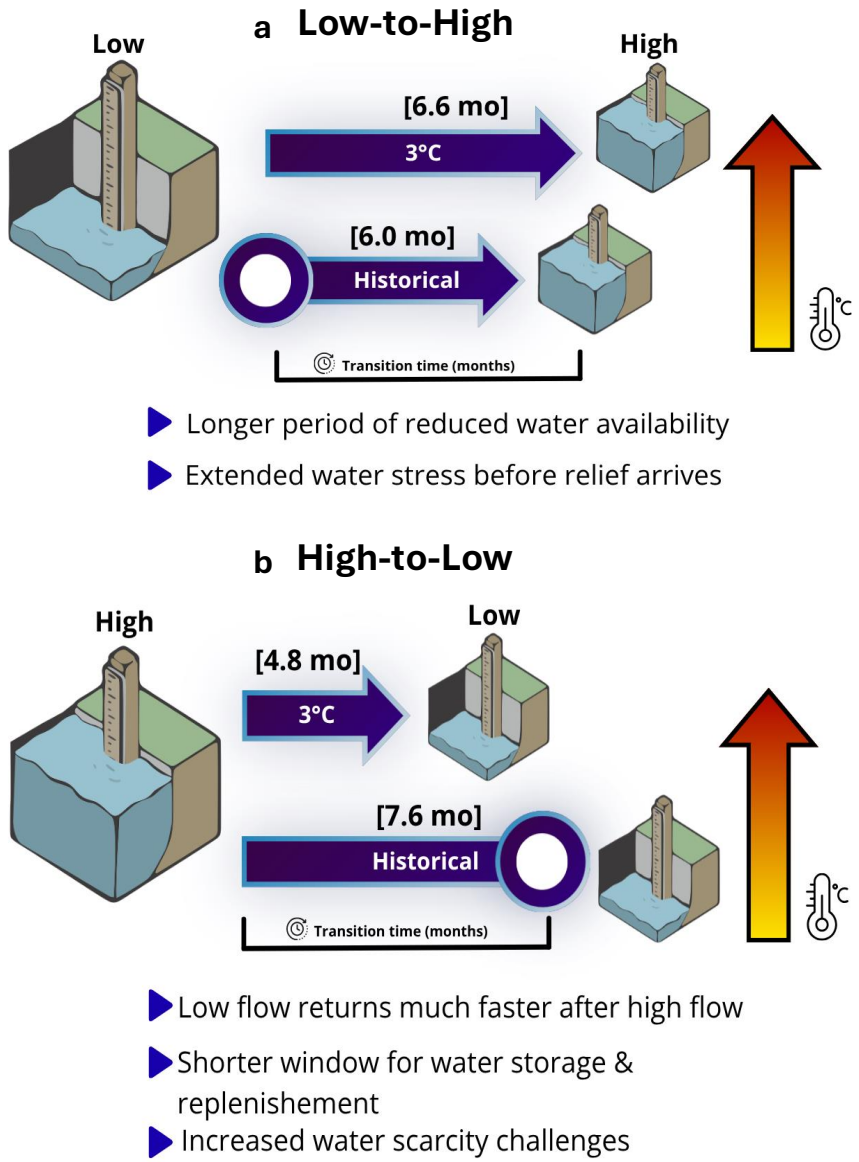


Fig. 5 | Changes in inter-episode transition times and implications. Illustration of transition time between low→high (**a**) and high→low (**b**) under a warming climate and possible implications.

Discussion

The projected increase in low-flow frequency across southern Europe and the Mediterranean, together with increasing high-flow frequency in northern Europe (Figs. 1 and 2), strengthens the established pattern of drying in the south and wetting in the north[33]. The north–south contrast is consistent with observed changes in European streamflow[3,7] and with previous projections of increasing low-flow pressure in MED[20,38]. The present analysis extends this understanding in two important respects. First, by examining low-flow and high-flow episodes within the same modelling framework, we show that opposing change directions co-occur locally across nearly half of the European land area (Fig. 3), revealing a spatially heterogeneous response. These divergent regional trajectories have important implications for water resource planning across Europe, where flood and drought risks are commonly managed under historical stationarity assumptions that are increasingly challenged by progressive warming[8]. Second, the transition-window analysis introduces a temporal dimension that has received limited quantification at the continental scale, measuring the interval between successive opposing low- and high-flow episodes and its response to progressive warming. Our continental-scale attenuation of sustained high-flow conditions differs from studies reporting regional increases in flooding in parts of central and western Europe[7,16].

This distinction reflects our use of SRI-based identification from monthly streamflow, which characterizes sustained high-flow conditions rather than short-duration flood peaks typically assessed from daily discharge maxima.

The 37% compression of the high→low transition time, from 7.6 months under historical conditions to 4.8 months at the warmest level (Fig. 4a), represents the sharpest hydroclimatic shift identified in this analysis. The complementary signal, a slight lengthening of low→high transition times in MED and CEU, compounds this asymmetry: not only do low-flow conditions return more quickly after high-flow episodes, but the interval of water stress before high-flow relief arrives also extends under warming, with potential consequences for agriculture, freshwater ecosystems, and municipal water supply. These two signals indicate an asymmetric tightening of transition windows in southern and central Europe: low-flow conditions return sooner after high-flow episodes, while high-flow relief arrives later after low-flow episodes. It should be acknowledged that our analysis does not account for irrigation, reservoir regulation, or land-use and land-cover changes, such as the conversion of forests and croplands to urban areas or shrublands, all of which can substantially modify streamflow regimes and the temporal sequencing of transitions between dry and wet conditions at the basin scale[52]. Accounting for these factors, together with higher-resolution regional modelling, will be critical

for improving estimates of transition times in heavily regulated catchments.

Beyond the median transition time itself, the distribution of high→low transitions signifies that the abrupt category becomes more prominent at 3°C across the entire domain (Fig. 4b). In contrast, low→high transitions show a more heterogeneous pattern, with both abrupt and gradual categories expanding. The moderate transition category becomes less common, decreasing from roughly 50% to 25% of river grid cells in both transition directions. This shift suggests a redistribution away from historically common transition times toward both shorter and longer transition classes. As a result, contraction of the moderate category across both transition types signals a shift from a historically unimodal toward a bimodal transition-time regime, in which the intermediate behaviour that water management systems are designed around becomes increasingly unrepresentative of actual hydrological conditions.

By examining $P-PET$ during transition windows (Supplementary Fig. 9), we find that the hydroclimatic balance between opposing streamflow conditions becomes increasingly water-limited under warming. Across Europe, $P - PET$ shifts toward more negative values, indicating that precipitation changes are generally insufficient to offset rising atmospheric water demand during transition windows.

The drying signal is particularly evident for high→low transitions, suggesting that enhanced evaporative demand can accelerate catchment drying after high-flow episodes and favour the onset of subsequent low-flow conditions. Regionally, this drying signal is strongest in central and Mediterranean Europe, whereas northern Europe shows weaker drying or more positive water-balance changes. Together, these results indicate that both declining precipitation and rising evaporative demand shape the pace of hydrological transitions under warming, although snow-driven processes may also influence transition timing in snow-dominated regions of northern and central Europe. These snow-related contributions are not explicitly isolated in the present diagnostic analysis.

Projected changes in streamflow sequencing may also have important implications for riverine ecosystems. Low and high-flow episodes affect riverine ecosystems through different mechanisms: low-flow periods reduce physical habitat availability and can stress aquatic communities, while high-flow pulses periodically reset channel conditions and facilitate the dispersal and recolonization of aquatic organisms[53,54]. As high→low transition times shorten and low→high transition times lengthen, the interval available for ecological recovery between contrasting flow conditions may become shorter, particularly in regions where low-flow conditions become more frequent. These changes could increase stress on

aquatic communities adapted to historical flow variability[55]. However, the ecological implications remain indirect in the present analysis and should be tested in future work using ecological response indicators.

Taken together, a conceptual illustration of transition times and their implications under climate warming is presented in Fig. 5. The shortening of high→low transition time, concurrent with a modest lengthening of low→high transition, narrows the window available for reservoir storage and groundwater replenishment before the next low-flow condition arrives, while simultaneously delaying relief from existing deficits, potentially amplifying the cumulative impacts of successive episodes[8]. Future work should integrate human water management, including reservoir operation and irrigation demand, with continental-scale hydrological projections, as regulated systems may amplify or buffer the transition-time dynamics identified here in ways that cannot be resolved at the resolution of the present analysis.

Our results demonstrate that progressive climate warming reshapes not only the frequency, magnitude, and duration of low- and high-flow episodes across Europe, but also temporal intervals separating them. Low-flow episodes intensify across MED, while high-flow episodes attenuate; in NEU, the opposite pattern

emerges, and these contrasting regional patterns increase with each additional degree of warming. At the continental scale, high→low transitions shorten from 7.6 months under historical conditions to 4.8 months at 3°C warming, representing a reduction of approximately 37%. By comparison, low→high transitions lengthen only marginally, from 6.0 to 6.6 months. These findings indicate that the timing of opposing streamflow episodes is an important dimension of climate change impacts on river systems. Adaptation and monitoring frameworks should therefore consider not only the magnitude, frequency, and duration of low- and high-flow episodes, but also the intervals between them.

Methods

Hydrological model setup and evaluation

We simulated streamflow across Europe at 0.125° resolution using mesoscale Hydrological Model (mHM)[28,29,56]. The hydrological model was forced with daily precipitation and mean, minimum and maximum temperature from E-OBS v31.0e[30] over 1960–2024, and we used the Hargreaves-Samani[57] potential evapotranspiration scheme. While the Penman-Monteith equation offers a more comprehensive physical framework, the Hargreaves-Samani method serves as a reliable, parsimonious alternative for large-scale drought analysis due to its minimal data requirements and its ability to yield hydrological trends and performance consistent with more complex formulations[58,59]. A 10-year spin-up (1950–1959) was applied to build this simulation. The mHM has been thoroughly evaluated across Europe for streamflow, soil moisture, and total water storage[58,60–63]. Accordingly, the model currently serves as the core framework of the German Drought Monitor[64].

We further evaluated historical mHM discharge simulations against daily observations from the Global Runoff Data Centre (GRDC, `https://grdc.bafg.de/`). We identified 1 721 stations with at least 30 years of records between 1960

and 2024 and catchment areas larger than 250 km^2. As the simulations were conducted at a resolution of 0.125°, only stations with observed basin areas differing by less than 15% from the simulated upstream area were retained. Stations were further filtered using a Kling-Gupta Efficiency (KGE[65]) threshold greater than -0.41, an established criterion for acceptable model performance based on previous studies[66], resulting in a final set of 1 153 stations (Supplementary Fig. 10a). The median KGE is 0.58 (daily) and 0.64 (monthly), indicating a good model performance (Supplementary Fig. 10b). Moreover, the Nash-Sutcliffe Efficiency (NSE[67]) also shows performance comparable to KGE (Supplementary Fig.10c), further supporting the ability of mHM to reproduce daily discharge variability.

Climate forcing, bias adjustment, and warming levels

Future projections were driven by the Inter-sectoral Impact Model Intercomparison Project Phase (ISIMIP3b[68,69]) climate data based on Coupled Model Intercomparison Project Phase 6 (CMIP6[70]) outputs from five global climate models: GFDL-ESM4, IPSL-CM6A-LR, MPI-ESM1-2-HR, MRI-ESM2-0, and UKESM1-0-LL. These GCMs are chosen to capture structural diversity while collectively representing the broader CMIP6 ensemble[71,72]. In particular, GFDL-ESM4, MPI-ESM1-2-HR and MRI-ESM2-0 models exhibit relatively low climate sensitivity,

whereas IPSL-CM6A-LR and UKESM1-0-LL exhibit higher climate sensitivity, resulting in distinct warming trajectories through 2100[32]. We did not use regional climate model projections because the analysis focuses on pan-European, monthly streamflow conditions under global warming levels and requires a consistent multi-GCM forcing framework. Moreover, recent work suggests that some regional climate model ensembles may underestimate European warming, which could affect the attribution of climate change impacts[73].

The standard ISIMIP3b forcings are bias-corrected using the W5E5 observational reference dataset[74]. Because the hydrological model evaluation in this study was based on E-OBS, we applied an additional E-OBS-based trend preserving bias-correction and statistical downscaling following the ISIMIP3b methodology[31]. This procedure generated meteorological forcing fields at 0.125° resolution, consistent with the mHM grid and with the observational reference used for model evaluation. For each GCM, projections under four Shared Socioeconomic Pathway scenarios (SSP1-2.6, SSP2-4.5, SSP3-7.0, and SSP5-8.5) were included. ISIMIP3b climate forcings were provided at 0.5° resolution and conservatively remapped to the 0.125° grid used by mHM. While the statistical downscaling does not explicitly resolve all topographic effects on local climate variability, this limitation is expected to have minimal influence on the continental-scale, monthly

streamflow characteristics analyzed here.

The study encompasses the pan-European domain, extending from the Iberian Peninsula to Scandinavia and from the British Isles to the Balkans. We also assess the regional hydro-climatic characteristics of low and high streamflow episodes by subdividing the domain into three macro-regions following the IPCC Special Report on Managing the Risks of Extreme Events and Disasters to Advance Climate Change Adaptation (SREX[75]) regions: Northern Europe (NEU), Central Europe (CEU), and Mediterranean (MED). These regions encompass the major hydroclimatic gradients in Europe. They range from the humid, snow-influenced climate of Scandinavia to the semi-arid, rainfall-dominated climate of the Mediterranean basin.

In assessing the impacts of different global warming levels, we selected periods corresponding to 1.5°C, 2°C, and 3°C increases in global mean temperature relative to the pre-industrial baseline. Since each GCM reaches these warming thresholds at different periods, model-specific time slices were extracted for each warming level. Following the ISIMIP3b temperature thresholds and time-slice framework, 31-year periods were defined around the year in which the global mean temperature reached each warming level under different SSP scenarios for

each GCM[76].

Standardized Runoff Index and percentile-based streamflow conditions

Streamflow conditions were characterized using the Standardized Runoff Index (SRI[34]), a dimensionless index that uses the deviation of streamflow from climatological norms by expressing anomalies in units of standard deviations relative to a reference distribution, which is similar to the Standardized Precipitation Index (SPI[77]). Unlike discharge-based thresholds or the Streamflow Drought Index[35], SRI reduces the influence of catchment size and mean-flow magnitude, enabling consistent comparison of streamflow anomalies across heterogeneous European catchments. In this study, SRI is computed from mHM-simulated streamflow, enabling the same percentile-based framework to be applied consistently across historical and future periods. This dimensionless metric enables consistent comparison of conditions across catchments and through time. SRI was computed at a 1-month timescale using streamflow simulated by mHM and driven by bias-corrected ISIMIP3b GCM forcings spanning 1850–2100, although only the 1960–2100 period was analyzed in this study. The monthly timescale was selected to capture rapid runoff responses to precipitation deficits. Our analysis is constrained to river grid cells with contributing areas exceeding 1 000 km^2, following

the approach of Marx et al. (2018)[9]. This excludes small headwater catchments and focuses on river reaches where flow conditions are more relevant for water resources management and less influenced by routing scheme uncertainties[9,78].

To account for the strong seasonality of European streamflow, probability distributions were fitted independently for each calendar month. For each river grid cell and month m (m=1–12), discharge values corresponding to that month during the E-OBS reference period (1960–2024) were extracted to estimate the parameters of a two-parameter Gamma distribution:

$$f(x;\,\alpha,\beta) = \frac{x^{\alpha-1}\,e^{-x/\beta}}{\beta^{\alpha}\,\Gamma(\alpha)}, \quad x > 0 \tag{1}$$

where $\alpha > 0$ and $\beta > 0$ are the shape and scale parameters estimated by maximum likelihood. The Gamma distribution was selected for its suitability in representing the positive-skewed, zero-bounded nature of streamflow data, consistent with its application in the original SRI formulation[34] and its established use in standardized streamflow more broadly[79]. The SRI reference period spans the overlapping windows between E-OBS observational records and the historical GCMs simulations, covering the climatology to the observed climate state, so that the projected SRI values (2025–2100) represent anomalies relative to E-OBS.

Once the monthly Gamma cumulative distribution functions (CDFs) were created, SRI was computed across the full 1960–2100 period. For each grid cell and time step, the non-exceedance probability (p), denoting the percentile rank of a given discharge value within the reference climatology, was evaluated from a month-specific Gamma CDF and then transformed to a standard normal deviation via the inverse of normal transformation:

$$\mathrm{SRI} = \Phi^{-1}(p) \tag{2}$$

where Φ^{-1} is the quantile function of the standard normal distribution. Both p and SRI were kept as outputs; however, following the approach of the Soil Moisture Index (SMI[80]), streamflow conditions were identified directly from p rather than from the standardized SRI values. Low streamflow conditions were defined as months where $p < 0.20$ and high streamflow conditions as months where $p > 0.80$, corresponding to discharge falling below the 20th and above the 80th percentile of the reference climatology. This percentile-based framework provides a direct measure of anomaly magnitude relative to the local reference.

Streamflow episode characteristics

We adopt a warming-level framework following the previous low streamflow studies[9] and the ISIMIP3b protocol, which categorizes three different global mean temperature thresholds (1.5°C, 2°C, and 3°C) above pre-industrial levels based on each GCM and SSP properties. For each GCM-SSP combination, we identify the 31-year window centred on the year when the global mean surface temperature reaches each threshold. Across the different SSP scenarios, results were pooled from all simulations that reached the same global mean temperature increase, allowing impacts to be assessed consistently across scenarios.

We calculated three characteristics for low-flow ($p < 0.2$) and high-flow ($p > 0.8$) conditions, where p denotes the monthly non-exceedance probability derived from the fitted reference distribution. An episode is defined as a sequence of consecutive months in which p remains below 0.20 for low-flow episodes or above 0.80 for high-flow episodes. Since each warming-level period comprises a 31-year window (372 months), magnitude and frequency are normalized to annual values to improve the interpretation of changes and enable comparison across warming levels. Magnitude is quantified as the mean annual cumulative percentile deficit for low-flow episodes, $\sum(0.20 - p)$, and percentile surplus for high-flow episodes, $\sum(p - 0.80)$. Frequency is defined as the mean annual number of discrete episodes over the 31-year period divided by 31 years. Duration represents

the mean length of individual episodes in months.

For validation, we compared mHM simulations driven by five bias-corrected GCMs with E-OBS-forced simulations over the 1960–2014 period, evaluating key episode characteristics: magnitude, frequency, and duration (Supplementary Fig. 11). For high-flow conditions, GCM-driven simulations demonstrate strong spatial correlations with E-OBS-driven simulations for frequency (median Pearson r = 0.65–0.73 across GCMs) and duration (r = 0.67–0.70), indicating that GCMs reliably reproduce the spatial patterns and temporal persistence of high-flow occurrence. Under low-flow conditions, similar performance is observed, with strong correlations for frequency (r = 0.65–0.73) and duration (r = 0.67–0.70). However, magnitude shows substantially lower agreement for both condition types (high-flow: r = 0.17–0.24; low-flow: r = 0.17–0.24). Despite these limitations in magnitude, the robust performance for frequency and duration provides confidence that projected changes in inter-condition temporal dynamics are not driven by model bias.

To analyze the relative changes in condition characteristics (Fig. 1), we compare each warming-level period with the historical reference period (1980–2010). Ensemble statistics are derived using a two-step aggregation procedure. First, for each GCM and warming level, changes are calculated separately for all SSP

simulations that reached that level, then aggregated using the median across SSPs. This produces one warming-level change estimate per GCM and grid cell. Second, multi-model summaries are calculated across the five GCM-level estimates, treating GCMs as independent realizations of the climate system. This aggregation procedure is applied consistently to derive spatial distributions and continental- and regional-scale summaries of episode characteristics.

Furthermore, we also analyse change directions in both low- and high-flows between the 3°C warming level and the historical period (1980–2010) using a paired statistical framework (Fig. 3). The Wilcoxon signed-rank test[81] was applied to each pixel to determine whether changes were statistically significant at the α = 0.05 level, appropriate for non-normally distributed hydrological data[82]. River grid cells were categorized into exclusive categories based on the sign and significance of changes in both low-flow (L) and high-flow (H) frequencies: L$+$, H$+$ (purple), L$+$, H$-$ (red), L$-$, H$+$ (blue), L$-$, H$-$ (green), and "no significant change" (grey, where $p \geq 0.05$ for at least one condition).

Signal-to-noise ratio

To assess the robustness of projected changes in streamflow conditions,

we employ signal-to-noise ratio (S2N), a widely used metric for quantifying projection confidence[83,84]. The S2N is defined as the absolute value of the multi-model ensemble change divided by the inter-model standard deviation. This metric quantifies whether the climate change signal emerged clearly from inter-model spread. We utilized the interpretation thresholds: S2N $>$ 1.0 indicates a robust signal where the ensemble mean exceeds inter-model variability; S2N between 0.75 and 1.0 indicates moderate confidence; and S2N $<$ 0.75 shows high uncertainty where the signal is obscured by model disagreement. The S2N was calculated separately for low- and high-flow projections across three warming levels, accounting for changes in condition magnitude, frequency, and duration.

S2N spatial distributions reveal systematic differences in projection confidence across characteristics and warming levels (Supplementary Fig. 4). High-flow projections consistently show higher model agreement than low-flow projections across all characteristics. Regarding frequency, high-flow has a larger mean S2N (1.90) than low-flow (1.29) at 3°C warming. Magnitude projections display the greatest contrast, with high-flow achieving exceptionally robust agreement (S2N = 2.66 vs 1.97 for low-flow), highlighting strong model consensus that thermodynamically driven extreme precipitation intensification drives both low- and high-flow intensity. Moreover, duration projections have moderate to high confidence

for both conditions at 3°C warming (S2N = 1.37 for high-flow, 1.49 for low-flow). Model agreement increases systematically with warming across all characteristics, with lower robustness at 1.5°C and stronger at 3°C, demonstrating that climate change signals emerge more clearly above internal variability at higher forcing levels. Geographically, high-confidence regions (S2N $>$ 1.25) at 3°C include the Mediterranean for low-flow and Northern Europe for high-flow, covering most European regions except Central Europe, which remains an uncertainty hotspot (S2N $<$ 0.75) for both conditions across all warming levels.

Inter-episode transition times

To characterize the temporal dynamics between contrasting hydrological streamflow episodes, we quantified the transition time between conditions as the duration between the end of one type and the beginning of the opposite type under different warming levels (Fig. 4a). Specifically, we addressed two directional transition metrics: (1) low$\rightarrow$high: the number of months from the end of a low-flow condition to the start of the next high-flow condition, and (2) high$\rightarrow$low: the number of months from the end of a high-flow condition to the start of the next low-flow condition. These temporal gaps were calculated as forward-only sequences. Transition times were computed separately within each warming-level period (historical 1980–2010

and future at 1.5°C, 2°C, and 3°C) to avoid temporal misalignment across different climate conditions. For each combination of grid pixel, GCM, SSP, and warming level, we identified all condition pairs that occurred within the 31-year period and calculated the median transition time across these pairs. The median transition time represents the typical waiting period between two contrasting episodes. Following our prior two-stage aggregation framework, we first computed the median across the four SSP scenarios within each GCM, then averaged across five GCMs to obtain the multi-model ensemble mean (one final value per river grid pixel per warming level).

From these transition windows, we also classified transition times into four categories based on percentile thresholds derived from the historical period (1980–2010), calculated separately for low$\rightarrow$high and high$\rightarrow$low transitions (Fig. 4b). The categories were defined as: Abrupt (transition time $<$ 10th percentile), Rapid (10th–25th percentile), Moderate (25th–75th percentile), and Gradual ($>$ 75th percentile). By applying these fixed historical thresholds to future warming levels, we quantified how the distribution of transition times shifted across categories, with changes in category membership indicating acceleration or deceleration of transitions relative to the historical baseline. This approach quantifies how the temporal spacing between opposing hydrological episodes evolves under progressive

warming, revealing whether climate change extends or compresses the interval between low- and high-flow conditions.

On the basis of an extended analysis, we quantified hydroclimatic conditions during transitions between opposing streamflow episodes using the monthly upstream catchment water balance, defined as $P - PET$, where P is precipitation and PET is potential evapotranspiration (Supplementary Fig. 9). For each routed river cell, monthly P and PET were calculated from the area-weighted catchment means of all upstream contributing cells draining to that river cell. This ensures that the climatic variables reflect the contributing drainage area of each routed river cell rather than the local grid-cell value. Transition windows were defined as the months occurring between the end of one episode and the beginning of the subsequent episode of the opposing type, separately for low-to-high and high-to-low transitions. Distributions were evaluated across all European routed river cells and divided into NEU, CEU, and MED.

Data availability

The data for hydrological modelling outputs are available on zenodo (DOI: 10.5281/zenodo.20441477). The data are currently under limited access and will be made

publicly available upon publication. The climate-forcing data from ISIMIP3b used to force mHM can be provided upon request.

Code availability

The code is available on Zenodo (DOI: 10.5281/zenodo.20441477). Right now, the access is limited, but we plan to open it for everyone to access post publication. The source of the mesoscale Hydrologic model used in the study can be found at `https://doi.org/10.5281/zenodo.8279545`.

Acknowledgements This research has been supported by the Grant Agency of the Czech Republic for project no. 26-23789S. R.Ke. was also funded by the Internal Grant Agency (Project no: 2026B0003), O.R. and R.Ke. also acknowledge the Research Excellence in Environmental Sciences (REES) project, both by the Faculty of Environmental Sciences, Czech University of Life Sciences Prague. D.Y. M.T., M.H, and O.R. also acknowledge support from the AdAgriF project (CZ.02.01.01/00/22_008/0004635). Computational resources to run the hydrological model mHM were provided by the e-INFRA CZ project, supported by the Ministry of Education, Youth and Sports of the Czech Republic

Competing Interests The authors declare no competing interests.

Author contributions R.Ke., R.Ku., and O.R. conceived the idea and designed the ex-

perimental framework. R.Ke. carried out the analysis. D.Y. helped with the initial model setup. R.Ke. wrote the initial draft with inputs from O.R., R.Ku., M.T., M.H., and A.A. All authors contributed to writing and editing the manuscript.

1. Götte, J. & Brunner, M. I. Hydrological drought-to-flood transitions across different hydroclimates in the United States. *Water Resources Research* **60** (2024).

2. Douville, H. *et al.* Water cycle changes. *Climate change 2021: The physical science basis. Contribution of working group I to the sixth assessment report of the intergovernmental panel on climate change* 1055–1210 (2021).

3. Gudmundsson, L. *et al.* Globally observed trends in mean and extreme river flow attributed to climate change. *Science* **371**, 1159–1162 (2021).

4. Sheffield, J., Wood, E. F. & Roderick, M. L. Little change in global drought over the past 60 years. *Nature* **491**, 435–438 (2012).

5. Gudmundsson, L. *et al.* Past and future change in global river flows. *Nature Reviews Earth & Environment* **7**, 7–23 (2026).

6. Stahl, K. *et al.* Streamflow trends in Europe: evidence from a dataset of near-natural catchments. *Hydrology and Earth System Sciences* **14**, 2367–2382 (2010).

7. Blöschl, G. *et al.* Changing climate both increases and decreases European river floods. *Nature* **573**, 108–111 (2019).

8. Kreibich, H. *et al.* The challenge of unprecedented floods and droughts in risk management. *Nature* **608**, 80–86 (2022).

9. Marx, A. *et al.* Climate change alters low flows in Europe under global warming of 1.5, 2, and 3 ℃. *Hydrology and Earth System Sciences* **22**, 1017–1032 (2018).

10. Demirel, M. C., Booij, M. J. & Hoekstra, A. Y. Impacts of climate change on the seasonality of low flows in 134 catchments in the River Rhine basin using an ensemble of bias-corrected regional climate simulations. *Hydrology and Earth System Sciences* **17**, 4241–4257 (2013).

11. Satzinger, U. & Bachmann, D. Conceptual approach for a holistic low-flow risk analysis. *Hydrological Processes* **38**, e15217 (2024).

12. Wada, Y., Van Beek, L. P., Wanders, N. & Bierkens, M. F. Human water consumption intensifies hydrological drought worldwide. *Environmental Research Letters* **8**, 034036 (2013).

13. Jongman, B. *et al.* Increasing stress on disaster-risk finance due to large floods. *Nature Climate Change* **4**, 264–268 (2014).

14. Van Loon, A. F. Hydrological drought explained. *Wiley Interdisciplinary Reviews: Water* **2**, 359–392 (2015).

15. Brunner, M. I., Swain, D. L., Gilleland, E. & Wood, A. W. Increasing importance of temperature as a contributor to the spatial extent of streamflow drought. *Environmental Research Letters* **16**, 024038 (2021).

16. Thober, S. *et al.* Multi-model ensemble projections of European river floods and high flows at 1.5, 2, and 3 degrees global warming. *Environmental Research Letters* **13**, 014003 (2018).

17. Blöschl, G. *et al.* Changing climate shifts timing of European floods. *Science* **357**, 588–590 (2017).

18. Gebrechorkos, S. H. *et al.* Warming accelerates global drought severity. *Nature* **642**, 628–635 (2025).

19. Lehner, B., Döll, P., Alcamo, J., Henrichs, T. & Kaspar, F. Estimating the impact of global change on flood and drought risks in Europe: a continental, integrated analysis. *Climatic Change* **75**, 273–299 (2006).

20. Samaniego, L. *et al.* Anthropogenic warming exacerbates European soil moisture droughts. *Nature Climate Change* **8**, 421–426 (2018).

21. Lobanova, A. *et al.* Hydrological impacts of moderate and high-end climate change across European river basins. *Journal of Hydrology: Regional Studies* **18**, 15–30 (2018).

732 22. Greve, P., Gudmundsson, L. & Seneviratne, S. I. Regional scaling of an-
733 nual mean precipitation and water availability with global temperature change.
734 *Earth System Dynamics* **9**, 227–240 (2018).

735 23. Matanó, A. *et al.* Compound and consecutive drought-flood events at a global
736 scale. *Environmental Research Letters* **19**, 064048 (2024).

737 24. Swain, D. L., Langenbrunner, B., Neelin, J. D. & Hall, A. Increasing precip-
738 itation volatility in twenty-first-century California. *Nature Climate Change* **8**,
739 427–433 (2018).

740 25. Chen, H. & Wang, S. Accelerated Transition Between Dry and Wet Periods in
741 a Warming Climate. *Geophysical Research Letters* **49** (2022).

742 26. Anderson, B. J. *et al.* What is a drought-to-flood transition? pitfalls and recom-
743 mendations for defining consecutive hydrological extreme events. *Hydrology*
744 *and Earth System Sciences* **29**, 6069–6092 (2025).

745 27. Van der Wiel, K., Batelaan, T. J. & Wanders, N. Large increases of multi-year
746 droughts in north-western Europe in a warmer climate. *Climate Dynamics* **60**,
747 1781–1800 (2023).

748 28. Samaniego, L., Kumar, R. & Attinger, S. Multiscale parameter regionaliza-
749 tion of a grid-based hydrologic model at the mesoscale. *Water Resources*
750 *Research* **46** (2010).

751 29. Kumar, R., Samaniego, L. & Attinger, S. Implications of distributed hydro-
752 logic model parameterization on water fluxes at multiple scales and locations.
753 *Water Resources Research* **49**, 360–379 (2013).

754 30. Cornes, R. C., Van Der Schrier, G., Van Den Besselaar, E. J. & Jones, P. D.
755 An ensemble version of the E-OBS temperature and precipitation data sets.
756 *Journal of Geophysical Research: Atmospheres* **123**, 9391–9409 (2018).

757 31. Lange, S. & Büchner, M. ISIMIP3b bias-adjusted atmospheric climate input
758 data (2021). URL `https://doi.org/10.48364/ISIMIP.842396.1`.

759 32. Lange, S. Trend-preserving bias adjustment and statistical downscaling with
760 ISIMIP3BASD (v1. 0). *Geoscientific Model Development* **12**, 3055–3070
761 (2019).

762 33. Intergovernmental Panel On Climate Change (Ipcc). *Climate Change 2021 –*
763 *The Physical Science Basis: Working Group I Contribution to the Sixth As-*
764 *sessment Report of the Intergovernmental Panel on Climate Change* (Cam-
765 bridge University Press, 2023), 1 edn.

766 34. Shukla, S. & Wood, A. W. Use of a standardized runoff index for characterizing
767 hydrologic drought. *Geophysical research letters* **35** (2008).

768 35. Nalbantis, I. & Tsakiris, G. Assessment of hydrological drought revisited. *Wa-*
769 *ter resources management* **23**, 881–897 (2009).

770 36. Marvel, K. *et al.* Twentieth-century hydroclimate changes consistent with hu-
771 man influence. *Nature* **569**, 59–65 (2019).

772 37. Huning, L. S. & AghaKouchak, A. Global snow drought hot spots and char-
773 acteristics. *Proceedings of the National Academy of Sciences* **117**, 19753–
774 19759 (2020).

775 38. Cammalleri, C. *et al.* Diverging hydrological drought traits over Europe with
776 global warming. *Hydrology and Earth System Sciences* **24**, 5919–5935
777 (2020).

778 39. Milly, P. C., Dunne, K. A. & Vecchia, A. V. Global pattern of trends in stream-
779 flow and water availability in a changing climate. *Nature* **438**, 347–350 (2005).

780 40. Ionita, M. & Nagavciuc, V. Changes in drought features at the European level
781 over the last 120 years. *Natural Hazards and Earth System Sciences* **21**,
782 1685–1701 (2021).

783 41. Kumar, R. *et al.* Multi-model assessment of groundwater recharge across
784 europe under warming climate. *Earth's Future* **13** (2025).

785 42. Aalbers, E. E., Van Meijgaard, E., Lenderink, G., De Vries, H. & Van Den Hurk,
786 B. J. J. M. The 2018 west-central European drought projected in a warmer
787 climate: how much drier can it get? *Natural Hazards and Earth System*
788 *Sciences* **23**, 1921–1946 (2023).

789 43. Padrón, R. S. *et al.* Observed changes in dry-season water availability at-
790 tributed to human-induced climate change. *Nature Geoscience* **13**, 477–481
791 (2020).

792 44. Boé, J., Somot, S., Corre, L. & Nabat, P. Large discrepancies in summer cli-
793 mate change over Europe as projected by global and regional climate models:
794 causes and consequences. *Climate Dynamics* **54**, 2981–3002 (2020).

795 45. Skalák, P. *et al.* The projected changes in the surface energy budget of the
796 CMIP5 and Euro-CORDEX models: are we heading toward wetter growing
797 seasons in Central Europe? *Journal of Hydrometeorology* **26**, 481–499
798 (2025).

799 46. Coppola, E. *et al.* Assessment of the European Climate Projections as Simu-
800 lated by the Large EURO-CORDEX Regional and Global Climate Model En-

semble. *Journal of Geophysical Research: Atmospheres* **126** (2021).

47. Spinoni, J., Naumann, G. & Vogt, J. V. Pan-European seasonal trends and recent changes of drought frequency and severity. *Global and Planetary Change* **148**, 113–130 (2017).

48. Hari, V. *et al.* The role of the North Pacific meridional mode on improved predictability of central European summer rainfall. *Environmental Research: Climate* **5**, 025024 (2026).

49. Spinoni, J. *et al.* Future global meteorological drought hot spots: a study based on cordex data. *Journal of Climate* **33**, 3635–3661 (2020).

50. Bevacqua, E. *et al.* Direct and lagged climate change effects intensified the 2022 European drought. *Nature Geoscience* **17**, 1100–1107 (2024).

51. Massari, C. *et al.* Evaporation enhancement drives the European water-budget deficit during multi-year droughts. *Hydrology and Earth System Sciences* **26**, 1527–1543 (2022).

52. Tyagi, M., Mishra, D., Mohanty, M. P. & Mishra, A. Compound Hydroclimatic Extremes Under Anthropogenic Influence: Transition Patterns and Population Exposure Risks. *Earth's Future* **14** (2026).

53. Poff, N. L. & Zimmerman, J. K. H. Ecological responses to altered flow regimes: a literature review to inform the science and management of environmental flows. *Freshwater Biology* **55**, 194–205 (2010).

54. Bunn, S. E. & Arthington, A. H. Basic Principles and Ecological Consequences of Altered Flow Regimes for Aquatic Biodiversity. *Environmental Management* **30**, 492–507 (2002).

55. Datry, T., Larned, S. T. & Tockner, K. Intermittent rivers: a challenge for freshwater ecology. *BioScience* **64**, 229–235 (2014).

56. Samaniego, L. *et al.* mesoscale hydrologic model (2017). URL `https://doi.org/10.5281/zenodo.1069203`.

57. George H. Hargreaves & Zohrab A. Samani. Reference Crop Evapotranspiration from Temperature. *Applied Engineering in Agriculture* **1**, 96–99 (1985).

58. Pohl, F. *et al.* Long-term daily hydrometeorological drought indices, soil moisture, and evapotranspiration for icos sites. *Scientific Data* **10**, 281 (2023).

59. Thakur, V. *et al.* Unveiling the impact of potential evapotranspiration method selection on trends in hydrological cycle components across Europe. *Hydrology and Earth System Sciences* **29**, 4395–4416 (2025).

60. Rakovec, O. *et al.* Multiscale and Multivariate Evaluation of Water Fluxes and States over European River Basins. *Journal of Hydrometeorology* **17**, 287–307 (2016).

61. Samaniego, L. *et al.* Hydrological Forecasts and Projections for Improved Decision-Making in the Water Sector in Europe. *Bulletin of the American Meteorological Society* **100**, 2451–2472 (2019).

62. Kumar, R. *et al.* Strong hydroclimatic controls on vulnerability to subsurface nitrate contamination across Europe. *Nature Communications* **11**, 6302 (2020).

63. Kettaren, R. *et al.* Storyline-based climate attribution reveals strong intensification of 2018–2022 multi-year droughts in europe. *Earth's Future* **14** (2026).

64. Zink, M. *et al.* The German drought monitor. *Environmental research letters* **11**, 074002 (2016).

65. Gupta, H. V., Kling, H., Yilmaz, K. K. & Martinez, G. F. Decomposition of the mean squared error and nse performance criteria: Implications for improving hydrological modelling. *Journal of hydrology* **377**, 80–91 (2009).

66. Knoben, W. J., Freer, J. E. & Woods, R. A. Inherent benchmark or not? comparing nash–sutcliffe and kling–gupta efficiency scores. *Hydrology and Earth System Sciences* **23**, 4323–4331 (2019).

853 67. Nash, J. E. & Sutcliffe, J. V. River flow forecasting through conceptual models
854 part i—a discussion of principles. *Journal of hydrology* **10**, 282–290 (1970).

855 68. Warszawski, L. *et al.* The inter-sectoral impact model intercomparison project
856 (ISI–MIP): project framework. *Proceedings of the National Academy of Sci-*
857 *ences* **111**, 3228–3232 (2014).

858 69. Lange, S., Quesada-Chacón, D. & Büchner, M. Secondary ISIMIP3b bias-
859 adjusted atmospheric climate input data (2024).

860 70. Eyring, V. *et al.* Overview of the Coupled Model Intercomparison Project
861 Phase 6 (CMIP6) experimental design and organization. *Geoscientific Model*
862 *Development* **9**, 1937–1958 (2016).

863 71. Rosa, L. & Sangiorgio, M. Global water gaps under future warming levels.
864 *Nature Communications* **16**, 1192 (2025).

865 72. Yadav, D. *et al.* Increasing spatial extent and frequency of flash drought in
866 Europe with each degree of global warming. *Environmental Research Letters*
867 **20**, 114046 (2025).

868 73. Schumacher, D. L. *et al.* Exacerbated summer European warming not cap-
869 tured by climate models neglecting long-term aerosol changes. *Communica-*
870 *tions Earth & Environment* **5**, 182 (2024).

871 74. Cucchi, M. *et al.* WFDE5: bias-adjusted ERA5 reanalysis data for impact
872 studies. *Earth System Science Data* **12**, 2097–2120 (2020).

873 75. Murray, V. & Ebi, K. L. IPCC special report on managing the risks of extreme
874 events and disasters to advance climate change adaptation (SREX) (2012).

875 76. Lange, S. & Büchner, M. ISIMIP3b bias-adjusted atmospheric climate input
876 data (v1.1) (2021).

877 77. McKee, T. B., Doesken, N. J., Kleist, J. *et al.* The relationship of drought
878 frequency and duration to time scales. In *Proceedings of the 8th Conference*
879 *on Applied Climatology*, vol. 17, 179–183 (Boston, 1993).

880 78. Forzieri, G. *et al.* Ensemble projections of future streamflow droughts in Eu-
881 rope. *Hydrology and Earth System Sciences* **18**, 85–108 (2014).

882 79. Svensson, C., Hannaford, J. & Prosdocimi, I. Statistical distributions for
883 monthly aggregations of precipitation and streamflow in drought indicator ap-
884 plications. *Water Resources Research* **53**, 999–1018 (2017).

885 80. Samaniego, L., Kumar, R. & Zink, M. Implications of parameter uncertainty
886 on soil moisture drought analysis in Germany. *Journal of Hydrometeorology*
887 **14**, 47–68 (2013).

888 81. Wilcoxon, F. Individual comparisons by ranking methods. In *Breakthroughs in*
889 *statistics: Methodology and distribution*, 196–202 (Springer, 1992).

890 82. Helsel, D. R., Hirsch, R. M., Ryberg, K. R., Archfield, S. A. & Gilroy, E. J.
891 Statistical methods in water resources. Techniques and Methods 4-A3, U.S.
892 Geological Survey, Reston, VA (2020). URL `https://doi.org/10.3133/`
893 `tm4a3`.

894 83. Hawkins, E. & Sutton, R. The potential to narrow uncertainty in regional cli-
895 mate predictions. *Bulletin of the American Meteorological Society* **90**, 1095–
896 1108 (2009).

897 84. Hawkins, E. & Sutton, R. The potential to narrow uncertainty in projections of
898 regional precipitation change. *Climate dynamics* **37**, 407–418 (2011).

Supplementary Files

This is a list of supplementary files associated with this preprint. Click to download.

- SupplementaryMaterials.pdf